

Ground and flight performance of the balloon-borne magnetic spectrometer AESOP-Lite

The AESOP-Lite collaboration

^a*Santa Cruz Institute for Particle Physics, Physics Department, University of California Santa Cruz, Santa Cruz, CA 95064*

^b*Bartol Research Institute, University of Delaware, Newark, DE 19716*

Abstract

The Anti-Electron Sub-Orbital Payload Low Energy (AESOP-Lite) is designed to explore the origin of the negative spectral index in the cosmic ray electron spectrum below 100 MeV through a series of balloon flights. The original entry telescope from the Classic LEE (Low Electron Energy) instrument has been directly integrated in AESOP-Lite. The instrument utilizes a gas Cherenkov and magnetic spectrometer configuration to identify particle type and determine the energy. The first flight took place May 15-21, 2018 from Kiruna, Sweden accumulating roughly 130 hours of exposure above 130,000 feet altitude before landing on Ellesmere Island, Canada. In this paper, we report on its design, calibration and performances. This includes the analyses of ground data taken during the integration of the detector before the flight. The observed muon charge separation from ground runs is discussed and compared to the expected performance of the spectrometer. The energy resolution from track reconstruction algorithms and the energy-dependent geometry factor are tested with Monte Carlo simulations. Finally, we present a brief overview of the 2018 flight and preliminary results of the detector performances in flight.

Keywords: cosmic rays - solar modulation - magnet spectrometer - balloon instrumentation

1. Introduction

The past decade has witnessed a new dawn in precision measurements of cosmic rays, with the launch of space-borne instruments such as PAMELA [1] and AMS-02 [2], as well as the more recent CALET, DAMPE, and ISS-CREAM experiments [3, 4, 5]. However, none of them has the sensitivity to study the lower range of the electron spectrum. Below 100 MeV, the effects of solar modulation at 1 AU can now be directly compared to the unmodulated VLIS (Very Local Interstellar Spectrum) probed by the Voyager spacecrafts [6]. For this purpose, we have designed, built, and flown a balloon-borne magnet spectrometer to measure electron and positron cosmic rays from 20 MeV to 300 MeV. AESOP-Lite successfully completed its first mission in May 2018, on a 5-day flight between Esrange, Sweden ($66^{\circ}89'N$) and Ellesmere Island, Canada ($78^{\circ}40'N$), on a NASA 40 million cubic foot, zero pressure, long duration balloon. Following that flight, work began on substantial upgrades to the instrument to prepare for a second flight, expected to take place in Antarctica in 2022 on a larger balloon capable of reaching greater altitude.

The AESOP-Lite instrument inherits its entry telescope from the well-traveled LEE (Low Electron Energy) payload [7]. Developed in the late 1960's at the University of Chicago, LEE provided pioneering measurements of low energy electrons [8] over the course of 23 flights, the last of which occurred in 2011. LEE's observations have highlighted the mysterious turn-up in the electron

spectrum around 80 MeV and the discrepancies between observations in the inner and outer heliosphere (see Fig. 3 in ref.[9]). No further conclusions can be reached until simultaneous measurements of electrons and positrons are made. Noteworthy to mention is the fact that the positron spectrum has never been resolved below 100 MeV, whereas in widely discussed results, PAMELA, Fermi-LAT, AMS-02 reported a positron fraction higher than the one predicted for a purely secondary model at energies above 1 GeV [10, 2, 11]. Thus, it was with the objective of extending measurements made by PAMELA and AMS-02 to the low-energy regime below 300 MeV that the AESOP-Lite mission was designed. In this paper we introduce the AESOP-Lite instrument and describe in some detail its detector system and capabilities. The focus here is on the upgraded instrument being prepared for the second flight, although information on the differences with respect to the original payload is also provided.

2. The detector system

The first consideration to reckon with in designing the new payload is the reduced weight required to reach higher altitudes on a balloon, in order to minimize the contribution of secondary cosmic rays produced in the residual atmosphere. Eliminating the LEE calorimeter aided that objective, and replacing it by a magnetic spectrometer provides discrimination between positrons and electrons. The AESOP-Lite instrument, consisting of an entry telescope

and the magnetic spectrometer, roughly retains the acceptance of the LEE instrument, thus maintaining a geometry factor that can provide good statistical accuracy, despite the low flux of primary electrons.

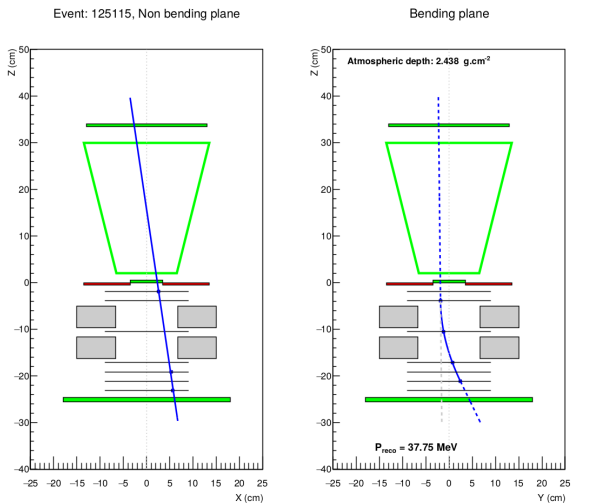


Figure 1: Event display of an electron candidate recorded during the 2018 flight. The triggers T1, T2, T3 and T4 were fired (in green) whereas no signal was seen in the guard (in red).

2.1. Pressure Vessel

2.2. Entry telescope

Fig. 1 shows a schematic cross section of the instrument. The entry telescope, taken from LEE, consists of three NE 102 A plastic scintillators (T1, T3 and Guard) and a gas Cerenkov detector (T2). T1 and T3 both aid in identifying singly charged relativistic particles, while T2 serves primarily to reject hadrons (protons make up $\sim 90\%$ of primary cosmic rays [12]). The Cerenkov counter is filled with C_3F_8 gas overpressured at 1.8 atm, to reject all particles with $\gamma = E/mc^2 \leq 15.7$ (corresponding to an electron or positron energy of approximately 8 MeV). Furthermore, it is sensitive only to downward-moving particles, thus rejecting the upward-going splash albedo present in the atmosphere. The combination T1-T2-T3 defines the geometry factor of the instrument ($15\text{cm}^2\text{sr}$), with a maximal acceptance angle of 27.5° from vertical. The coincident signal T1-T2-T3 is used in flight as the main instrument trigger, but two additional prescaled triggers that do not require a Cerenkov signal run in parallel with the main trigger.

The guard counter (G), used strictly offline, serves to veto events with particles produced by showers inside the apparatus, while the plastic scintillator T4, placed at the very bottom of the instrument, detects particles that have completely penetrated the instrument. T4 is also used together with T1 to measure time-of-flight (TOF), primarily to aid in distinguishing downward going positrons from a background of upward going electrons.

The fact that the same entry telescope was used in LEE flights provides a means to cross-calibrate the AESOP-Lite absolute electron fluxes with previous measurements. This similarity with the ancestral LEE instrument ends there however: the novelty of AESOP-Lite lies in the use of a magnetic spectrometer capable of distinguishing positrons from electrons, replacing the calorimeter previously employed, which was insensitive to the charge sign.

2.3. Custom Data Acquisition Electronics

The first AESOP-Lite flight utilized legacy electronics from LEE as part of the cross-calibration between the two instruments. The legacy boards were designed around 8 Bit MC68HC architecture microcontrollers and consisted of one readout board, three pulse-height analyzer boards (one main and two secondary), two counter boards, a power relay board and two high voltage control boards. An additional board to manage the trackers was created by repurposing an existing board design by adding LVDS communication. All boards connected to a backplane with shared power lines, a shared clock, a command broadcast UART line, and lines for a unidirectional communication protocol, similar to SPI, the readout board uses to collect data from other boards. For the second AESOP-Lite flight the electronics are upgraded to process additional triggers sources, reduce latency and jitter in triggers, determine direction of particles, reduce noise, optimize for multiple factors, increase flexibility, and modernize. The new data acquisition (DAQ) board includes two Cypress CY8C5888AXQ-LP096 PSOC chips, referred to as the “Main PSOC” and “Event PSOC”. The Main PSOC implements the legacy functionality of the readout board communications and one counter board that includes reading two barometers connected to the outside atmosphere. The Event PSOC implements the legacy functionality of three pulse-height analyzer boards, one counter board that includes signals related to events, and the tracker management board with LVDS communication to the trackers. The PSOCs primarily use reconfigurable SPI buses to communicate with each other and other components on board. The DAQ board regulates multiple voltages for use in analog and digital circuits, including a digital 5V that is shared on the backplane, replacing the standalone 5V supply. A shielded section at one end of the board houses the five pulse-height analysis channels. Each PSOC has an I2C bus to connect to sensors and other components including a third barometer for internal readings. The Main PSOC I2C bus is connected to sensor on the new tracker power board, which now has power outputs for eight tracker board, increased from seven. Three LEE legacy boards, power relay board and two high voltage control boards, are included in the upcoming flight since their basic power functionality did not need an upgrade. Furthermore, we replaced the backplane of the electronics crate by a new 4-layer board design, with full power and ground planes, in which the clock signal is distributed by LVDS, instead of 5-volt single-ended CMOS, in order to reduce electronic noise

145 that might affect the sensitive tracker electronics. The new DAQ board was developed on the LEE backplane as
150 a replacement in the same slot as the legacy readout board. The Main PSOC firmware can be configured in a legacy
155 backplane mode and communicate with legacy boards if
160 that mode should be need in the future.

2.3.1. Pulse-Height-Analysis

The five channels that process PMT signals are identical in design but have different gains, due to the differences in signals between the scintillators and Cerenkov
165 detector and also due to the higher-gain, faster PMTs used for T1 and T4 to make the TOF measurements.
170 Each analog channel begins with a charge-integrating inverting preamplifier implemented from one channel of an LTC6248 180 MHz dual operational-amplifier chip in an
175 8-lead MSOP package. For T3 and the Guard, negative feedback of 36 pF in parallel with 62 kOhms gives a peak at about 50 ns of 26 mV per pC of input charge. For T1 and T4 the feedback components are 220 pF and 10.2 kOhms,
180 giving a gain of 4.7 mV/pC, and for T2 components of 100 pF and 22.1 kOhm give a gain of 10 mV/pC. The LTC6248 is powered by ± 2.5 V supplied by an LT3032
185 dual linear regulator.

The preamplifier outputs are viewed by discriminators that generate trigger signals. The T2 channel discriminator
190 is implemented by an LTC6752 comparator, with a threshold supplied by an AD5602 12-bit DAC that is on a I²C bus mastered by the Event PSOC. The other four discriminators are implemented by the four comparators and four 8-bit voltage DACs included in the Event-PSOC
195 chip.

Each preamplifier is also coupled to an inverting shaping amplifier, using the second channel of the LTC6248 chip, by a 2 nF capacitor in series with 200 Ohms. The amplifier feedback is 220 pF in parallel with 1.21 kOhms,
200 giving a voltage gain of about -2.5 and peaking time of about 320 ns. Each shaping-amplifier output goes into a peak detector made from both channels of an LTC6244 amplifier.[13] One of the two op-amps is configured as unit-gain inverting amplifier that drives current onto a
205 2 nF capacitor with the aid of an NPN transistor from a BCM847 matched pair. The matching transistor sits in the amplifier feedback loop to cancel the effect of the base-emitter voltage drop. The second amplifier is a high-input-impedance non-inverting amplifier with gain of 2 for
210 T2, T3, and Guard, or 1.6 for T1 and T4, which buffers the capacitor voltage to the output, where it is viewed by the ADCs.

Each peak-detector capacitor has a 1 megOhm capacitor in parallel, giving it a reset time constant of 2 ms. After each discriminator threshold-crossing, however, the Event PSOC sends a digital signal to five BS170F MOSFETs to short all of the peak detector capacitors to ground, thus
215 resetting them for the next event.

In the first iteration of the data-acquisition board, the two 12-bit SAR ADCs internal to the Event PSOC were
220

used to digitize the peak-detector voltages. However, it proved to be impossible for us to make that work correctly. When the electronics were stimulated by constant-size test pulses, the digitized results showed spreads that were factors of 5 to 10 larger than expected, with a lot of missing codes. That was true even when we removed all digital activity, within the chip and outside of it, that was not essential for digitizing the signal. We also tried various different analog routing schemes within the PSOC, internal versus external reference, and more, all to no avail. Finally we made a second iteration of the board that included five AD7091R 12-bit SAR ADC chips and a single LT1460 3.3 V reference, and that worked very well, with the full 12-bit precision.

The ADCs are read out by the Event PSOC via the same SPI bus used to control the TOF TDC chip. All of the readout sequencing, including resetting the peak detectors, is controlled by two digital modules coded in Verilog and programmed into the digital fabric of the Event PSOC.

2.4. Data Readout and Commanding

Data readout and command functionality utilize one USB and four RS-232 communication lines. Two RS-232 boards are used to convert LVDS signals from the DAQ board to RS-232. Separate boards are used for to reduce noise on DAQ, edge space for DE9 connectors, and for redundancy. Each board has a high-rate channel (currently set to 19200 baud) and a low-rate channel (1200 baud). The two low-rate channels are received commands from and send periodic small data packets to the two redundant CSBF flight computers. For the upcoming flight, one of the high-rate channels will be connected to a Slerj SSR-LC Single Channel Data Logger [14] to record instrument data. The other high-rate channel can be configured to meet the requirements of a of an ultra-high frequency (UHF) line of sight (LOS) transmitter like the one used in the 2018 flight. However, no such transmitter is planned for use in the upcoming flight. Each RS-232 board connects to the DAQ board via a CAT5 cable. For the upcoming flight, the USB on the DAQ board will be connected to a Raspberry Pi 3b single board computer. The Raspberry Pi receives the same instrument data as the high-rate RS-323 and uses a custom program to save a copy to the onboard microSD card and send it to one or more UDP streams. In the upcoming flight, the two UDP streams will be sent utilizing Ethernet over Telemetry (EVTM) for line-of-sight range and Iridium Pilot broadband satellite terminal for whole flight communication.

2.4.1. Time of Flight

The T1 and T4 signals each go to one channel of an LT1715 fast dual comparator, in addition to going into the pulse-height-analysis circuit. Each negative threshold is provided by an AD5602 12-bit DAC followed by an OP07D op-amp configured as a voltage inverter. The Event PSOC programs the thresholds via the I²C bus.

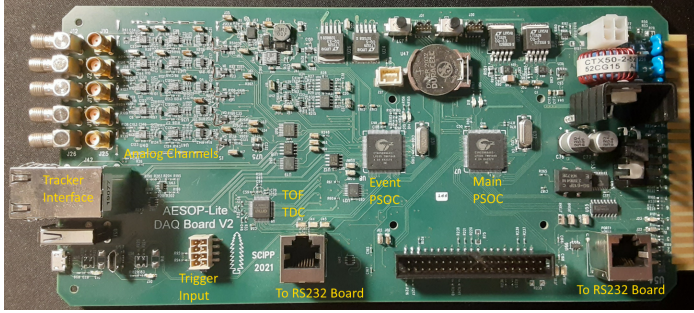


Figure 2: The data acquisition board.

The LVDS comparator outputs go directly to an AS6501 dual time-to-digital converter chip (TDC). The TDC chip's detailed internal configuration is established by way of its SPI interface with the Event PSOC. The Event PSOC also provides to the TDC a 12 MHz time-reference clock and a 24 MHz system clock. Each channel of the TDC outputs two LVDS digital signals: a frame and a bit stream. At the beginning of each frame, corresponding to a TDC "stop" event (initiated by a comparator threshold crossing), the Event PSOC clocks into an internal shift register 16 bits of the reference clock count and 16 bits of TDC₃₀₀ information on the time of the comparator signal between reference clock counts. Every 5 ms the Event PSOC sends an SPI command to reset the TDC reference-clock counters, before they roll over. The Event PSOC internal time at which the reference counter is reset, combined with the reference clock count and the TDC stop time, gives an absolute time of 10 ps precision for each TDC stop event.

As soon as a 32-bit shift register is filled with information on a TDC stop event, the bits are loaded into PSOC memory via DMA. Except for using the same reference₃₁₀ clock, the two TDC channels operate independently. Furthermore, the TOF information flows into memory independent of the instrument trigger. When there is a trigger and the Event PSOC reads data from the various detectors, it has to scan through the TOF stop events buffered₃₁₅ in memory to look for events in the two channels that match the trigger time stamp and are very close together in time. The minimum time difference found between the two channels is taken to be the TOF, which is stored to 10 ps precision but has a resolution of more like 1 ns rms.₃₂₀

2.5. Magnetic spectrometer

The magnetic spectrometer consists of a tracking system composed of eight planes (seven planes prior to the upgrade) of silicon strip detectors (SSDs) and a Halbach₃₂₅ ring dipole magnet[15], which produces a field that points primarily in the $+x$ direction (see Fig. 1). The average B_x in the symmetry plane is 0.33 T. Across the magnet bore, in the symmetry plane, it varies by as much as 3.2%, whereas the variation within the bore along the symmetry axis is 27%. The integral of B_x along the symmetry axis from $z = -20$ cm to $z = +20$ cm is 0.057 T m.

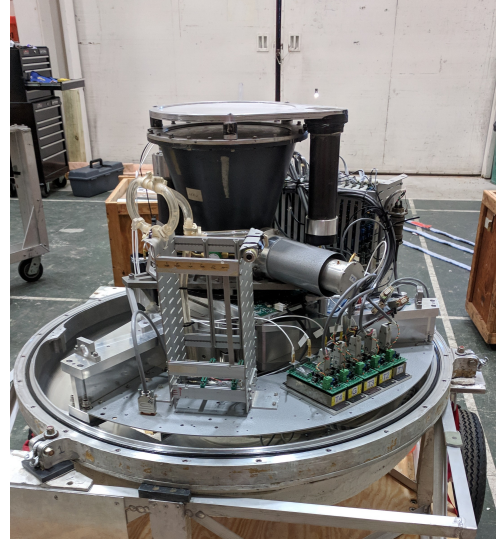


Figure 3: Photograph of the AESOP-Lite instrument with the pressure-vessel "shell" removed.

The detectors are arranged in an *xy*-configuration, with five layers in the bending plane to measure the particle deflection, and three layers to view the trajectory in the non-bending plane. The split magnet design allows a tracking layer to be easily placed in the bending view at the center of the field, thus optimizing the momentum resolution.

The SSDs were custom designed and manufactured by Hamamatsu Photonics for the Large Area Telescope (LAT) of the NASA Fermi gamma-ray telescope mission [16]. Each sensor is an 8.95×8.95 cm², 400 μ m thick single-sided detector, with a strip width of 56 μ m and pitch of 228 μ m. A bias potential of ~ 120 V is applied across the *n*-type bulk material between the strips and the back-side electrode. Each *p*-type strip implant is AC-coupled to an aluminum strip just above and biased through a ~ 50 M Ω polysilicon resistor.

Aluminum strips and bias rings on pairs of sensors are wire bonded together to form ladders. The ladder strips are then wire bonded to aluminum traces on single-layer glass "pitch-adapter" circuits, which in turn are wire bonded to the readout integrated circuits. The positive bias voltage is applied directly to the backs of the sensors through conductive epoxy that attaches them to printed circuits that are cut out under the sensor active areas. Epoxy adhesive is applied to the joint between ladders after they are mounted, to protect them from shock during transportation and during parachute deployment. Fig. 3 shows a photograph of one of the eight tracker modules.

Each SSD strip is connected to a channel of one of the twelve 64-channel readout ASICs (Application Specific Integrated Circuit) [17], which were designed for the tracking readout of a prototype proton-CT scanner [18]. The chips are capable of more than ten times faster readout than those used in the Fermi LAT, which is not relevant to the low rates of AESOP-Lite, but they are also easier to



Figure 4: Photograph of one of the eight tracker modules. The SSD sensor strips are wire-bonded to form two-sensor ladders. The 768 channels are wire bonded to 12 readout ASICs via glass-substrate pitch-adapter circuits.

use and configure for this application. Each channel has a charge-sensitive amplifier followed by a shaping amplifier and discriminator. The shaping time constant has two 335 digitally configured settings and can also be adjusted by external resistors. For AESOP-Lite it is about a microsecond, resulting in an effective noise charge at the input of 3370 ~ 1200 electrons and a signal-to-noise ratio for minimum ionizing particles of ~ 27 .

The discriminator thresholds are set by a single internal DAC per chip. The discriminator output goes into a logical OR of all channels to provide an asynchronous 335 trigger output, and it is also sampled by the clock within an adjustable window and buffered pending a trigger decision. Hits above threshold are output by command as a list of strip clusters. Two 64-bit masks can be used to remove individual channels from respectively the trigger 380 output and the data flow.

The cluster lists are buffered for up to four events (although this buffering is not used for AESOP-Lite) and delivered by LVDS (Low-Voltage Differential Signaling) in twelve serial streams to a Xilinx Spartan-6 FPGA operating with the same 10 MHz clock as used by the ASICs. 355 The FPGA firmware configures and monitors the tracker, and the seven FPGAs work together to deliver the data to the FPGA of the top, master board, which then sends the data by a 115200 baud UART to the AESOP-Lite data acquisition.

The FPGAs communicate with each other at 10 million 360 bits per second by LVDS signals transmitted over CAT-5 cables. They also sample the ASIC trigger signals, make a logical OR of the signals from the twelve chips, and pass the results from one bending-plane board to the next and from one non-bending-plane board to the next. The Event 390

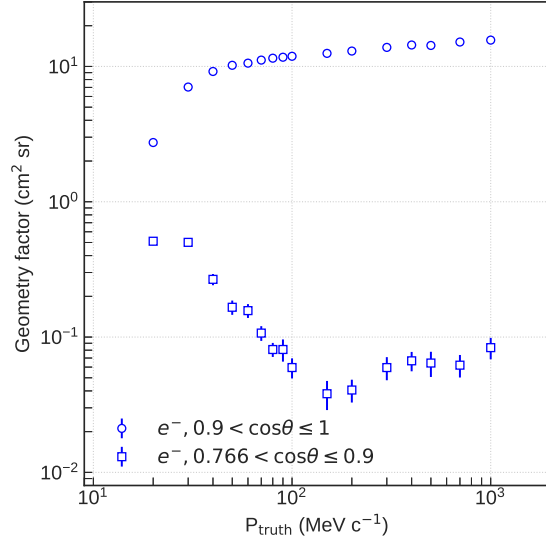


Figure 5: (Left) Model of the AESOP-Lite instrument viewed in the graphical interface Flair. (Right) Simulated post-trigger geometry factor for electrons. The calculations are made for two ranges of incident angle θ .

PSOC thus receives two trigger coincidence signals, one from the bending view and one from the non-bending view. The tracker trigger can be changed by command to be an AND or an OR of those two signals.

Prior to the upgrade, the coincidence signal from the AESOP-Lite scintillators proved to be too slow, with too much jitter, to trigger the tracker reliably, requiring use of the internal tracker trigger for all data acquisition. The tracker held its data following each tracker trigger until a “go” signal was received by the tracker master board from the T1-T2-T3 coincidence. If five microseconds passed with no “go” signal received, then the tracker data were discarded. The upgraded scintillator readout electronics provide a sufficiently fast trigger for the tracker, so that the internal tracker trigger is no longer needed. However, it is retained as a prescaled secondary trigger used to acquire an unbiased subset of the abundant proton tracks that pass through the instrument.

There is no buffering of events in the readout system, despite the fact that such a capability is built into the ASICs. Instead the trigger is disabled until the event readout is completed, a simple solution that is allowed by the low cosmic-ray rate.

3. Instrument performance

3.1. Geometry factor

Following the method outlined in [19], we use Monte Carlo simulations to determine the geometry factor of the AESOP-Lite instrument for each particle type studied and each zenith-angle bin. The right panel of Figure 5 shows

395 the acceptance for electrons when imposing the flight trigger requirements: a signal in T1, T2 and T3, and a simulation of the internal tracker trigger. As expected, the geometry factor grows with increasing momentum, as the deflecting effects of the magnetic field are mitigated: the
 400 acceptance is $\sim 7 \text{ cm}^2 \text{ sr}$ at $30 \text{ MeV}/c$ and $\sim 14 \text{ cm}^2 \text{ sr}$ at $300 \text{ MeV}/c$.

3.2. Track Reconstruction

Once an event has successfully passed the selection criteria of the online trigger coincidence (for instance T1–T2–T3), it is first processed with a pattern recognition (PR) routine that selects hits belonging to a same track: *i*) in the non-bending view, the algorithm fits all possible lines between the top-most and bottom-most layers, and chooses the track that minimizes the χ^2 ; *ii*) similarly in the bending view, a parabola is fit to all possible configurations of hits in the four layers of the plane and the best fit is chosen. From the radius of curvature of the parabola, the momentum of the particle can be inferred. The value from the PR fit is then used to initialize the final reconstruction method. However, for this preliminary analysis, the PR routine was used as the primary reconstruction technique. A Kalman Filter [20] and an algorithm that employs simplex minimization of Runge-Kutta integrations have also been developed and are being tested for track fitting. Figure 1 illustrates the parabola fit and straight line fit as seen in solid blue lines in our event display tool. The dashed lines in the bending plane panel indicate the incoming and outgoing trajectories of the particles, assuming no scattering or interaction in the detector.

425 Since the distribution of the reconstructed inverse momentum—and not the momentum itself—follows a normal distribution, we derive for each reconstructed energy and bin in zenith angle, θ , the $1/p_{\text{reco}}$ distribution and fit it to a Gaussian function. The reconstruction p.d.f. also contains
 430 the information of the particle’s energy loss, as it will have traversed the pressure vessel wall, the scintillators T1 and T3, as well as the C_3F_8 Cherenkov gas prior to reaching the spectrometer. The resolution, bias, and efficiency of the reconstruction are thus parametrized for 16 energies
 435 for electrons and positrons. Some examples of p.d.f. are shown in the left panel of Fig. 6. The parameters of the fits are then individually and linearly interpolated to extend the knowledge to the entire energy range of the instrument. The same method is used for all particle types.

440 On average, we estimate the compounded energy loss to be $\sim 4 \text{ MeV}$, a value independent of the energy of the incident particle. The center panel in Figure 6 presents the resolution of our current reconstruction algorithm for electrons: it is about 11.5% at $30 \text{ MeV}/c$ and 13.5% at
 445 $300 \text{ MeV}/c$. The right panel in Figure 6 shows the efficiencies (post-trigger) of the selection applied to the hits occupancy in the tracker (a number of hits between 5 and 12), and the PR. The distribution shows that the highest efficiency is in our range of interest, i.e., between 30 and
 450 $100 \text{ MeV}/c$. Similar results are obtained for positrons.

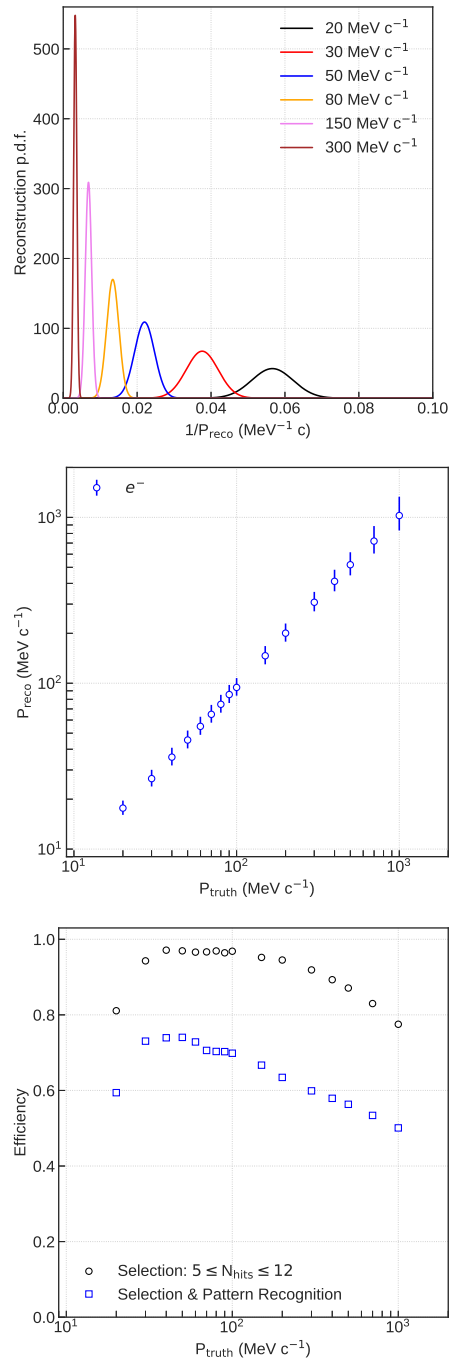


Figure 6: (Left) Reconstruction probability density function for the electrons (incidence: $0.9 < \cos \theta < 1$). (Center) Resolution of the momentum reconstruction for electrons and (right) the associated efficiency.

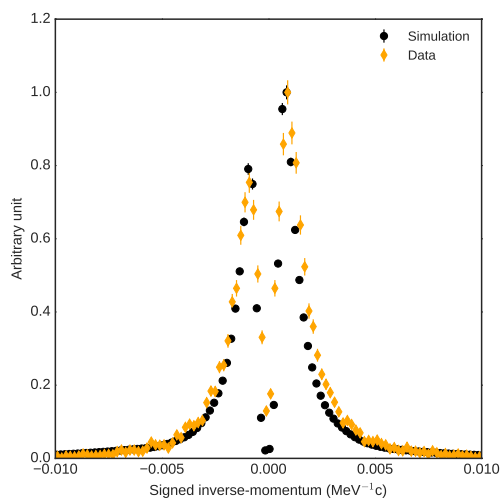


Figure 7: Ground level distribution of the signed inverse⁴⁸⁵ momentum of muons as measured by AESOP-Lite in May 2019 at Esrange (orange diamonds) and estimated by simulation (black markers). Histograms are normalized to 1 at their maximum.

490

3.3. Ground runs

Ground runs with different trigger configurations were performed in Esrange prior to the flight. In particular, the simple coincidence of signals in the scintillators T1 and T4 allowed us to accumulate tracks in the spectrometers without vetoing any contributions from muons with⁴⁹⁵ insufficient energy to produce Cherenkov light in T2. We applied an anti-coincidence offline veto on T2 to select only the low energetic muons and test our ability to separate and identify positively and negatively charged particles. Figure 7 shows the measured distribution of the signed⁵⁰⁰ inverse-momentum. We compare it with simulated distributions that combine a realistic spectrum of Galactic Cosmic Rays at the top of the atmosphere, atmospheric interaction shower [?], and the performances of detection presented previously in this paper. The charge separation is observed with a higher contribution of the positively charged muons as expected, as a majority cosmic rays is positively charged. There is a reasonably good agreement between calculations and observations. The measured double peaks are located at the same signed inverse⁵¹⁰ momentum as simulated. However they are slightly wider than the expected peaks. This possibly indicates an overestimation of the calculated reconstruction resolution in the momentum range of several hundreds of MeV/c.

470
475
480
485
490
495
500
505
510
515
520

Uncertainties on the simulated muon spectrum at ground level cannot be neglected as a possible explanation. The peak-to-peak atmospheric muon charge ratio μ^+/μ^- is observed at 1.33 ± 0.07 (statistical uncertainty only), a value close to the measurement made by CMS below 100 GeV [21].

If, however, we require offline for T2 to be have been fired, the distribution is then dominated by low-energy

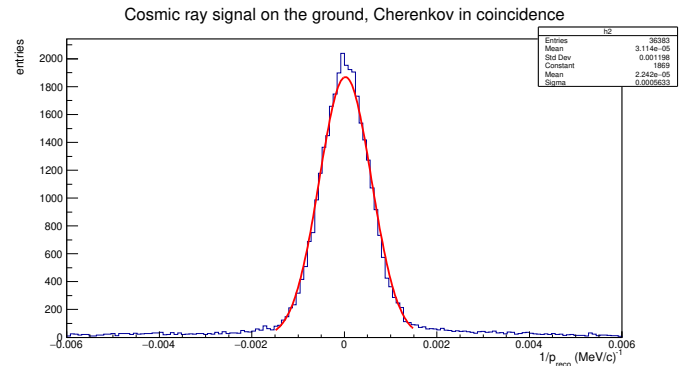


Figure 8: Cosmic ray signal on the ground with T1-T2-T3-T4 requirement

electrons and positrons, as well as high-energy muons that appear as quasi-straight tracks (7 mrad deflection at 1.5 GeV). We can determine Maximum Detectable Rigidity (MDR) of the spectrometer by fitting a Gaussian function to the inverse momentum signal (Fig. 7), from which we calculate the MDR = $1/3\sigma_{\text{reso}} = 590$ MV. This rigidity range is amply separated from the background of highly relativistic protons encountered during flight. The cosmic ray events collected from ground runs were processed with track reconstruction algorithms developed with Monte Carlo simulations.

4. 2018 campaign and future prospects

AESOP-Lite launched from Esrange, Sweden for a 133 hour-long flight at an average altitude of 41 km. It landed on Ellesmere Island, Canada. The northerly trajectory of the payload (see Fig. 7) allowed to survey regions of low (below 0.2 GV) rigidity cutoff (the minimum rigidity a particle must have to enter the magnetosphere at a certain location).

In flight configuration, the instrument was enclosed in an aluminum pressure vessel covered by a polyurethane foam of 2.5 cm thickness. The total weight of the gondola, including the batteries and solar panels, was 390 kg. The payload launched with an additional 270 kg of ballast.

Calibrations of the two barometers of the AESOP-Lite instrument were performed in Palestine, Texas and Esrange, Sweden prior to the AESOP-Lite maiden flight. The barometers were used in flight to record the pressure outside the shell, measuring the float altitude and atmospheric overburden. Accurate knowledge of the altitude is necessary in order to compare flight data with a MC shower model of the cosmic-ray secondary background.

Three self-activating heaters maintained the temperature inside the shell in the neighborhood of 20° C. Four 100 Watt solar panels provided power to the instrument in flight, which used 73 W with the heaters on. Three telemetry channels were used for monitoring the good health of the apparatus and receiving data in live time: S-band

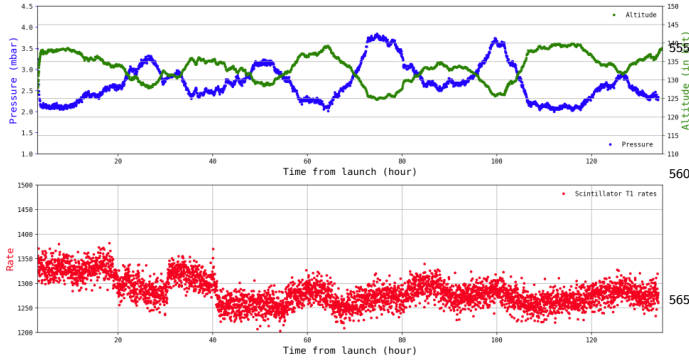


Figure 9: Top panel shows the pressure and altitude flight profile. As the sun sets below the horizon, the volume of the balloon shrinks and its altitude drops, which explains the diurnal variations. Bottom panel illustrates the time profile of T1 scintillator count rate, revealing diurnal variation in the cosmic ray flux

(frequency range of 2 to 4 GHz), line-of-sight (for a surprisingly long 40 hours), low-rate Iridium (for housekeeping information), and high-rate Pilot Iridium. Each one was doubly redundant, with two operative communication lines: COMM 1 and COMM 2. To maximize data transmission rates, UDP (User Datagram Protocol) was used in preference over TCP (Transmission Control Protocol). Because the telemetry transmission incurred almost 50% loss on average over the flight, three black-box recorders were installed on the gondola to safely record all data.

The AESOP-Lite instrument and data recorders were recovered in good shape. Preliminary inspection indicated that the instrument operated at the expected efficiency. Analysis of flight data and further MC simulations are ongoing to determine the detector's efficiency and derive the flux of primary electrons and positrons. Upcoming plans include refurbishing the instrument and upgrading the entry telescope's electronics in preparation for future flights, to explore different solar modulation epochs.

5. Acknowledgments

We would like to thank Matthew Collins, Forest Martinez-Mckinney, and Yang Zhou for their help in the design, construction and integration of the instrument. We thank Chris Field and the CSBF for their support during the integration period in Palestine, Texas, and for the successful balloon flight. We thank Esrange for their support during the flight campaign. This work is supported by the NASA award 80NSSC19K0746.

550 References

References

- [1] M. Casolino, et al., Launch of the space experiment PAMELA, Advances in Space Research 42 (3) (2008) 455–466. doi: 10.1016/j.asr.2007.07.023. URL <http://www.sciencedirect.com/science/article/pii/S0273117707007831>
- [2] M. Aguilar, others, (AMS Collaboration), Electron and Positron Fluxes in Primary Cosmic Rays Measured with the Alpha Magnetic Spectrometer on the International Space Station, Physical Review Letters 113 (12). doi:10.1103/PhysRevLett.113.121102. URL <https://link.aps.org/doi/10.1103/PhysRevLett.113.121102>
- [3] O. Adriani, others CALET Collaboration, Energy Spectrum of Cosmic-Ray Electron and Positron from 10 GeV to 3 TeV Observed with the Calorimetric Electron Telescope on the International Space Station, Physical Review Letters 119 (18). doi:10.1103/PhysRevLett.119.181101. URL <https://link.aps.org/doi/10.1103/PhysRevLett.119.181101>
- [4] F. Gargano, DAMPE collaboration, The DAMPE experiment: 2 year in orbit, Journal of Physics: Conference Series 934 (2017) 012015. doi:10.1088/1742-6596/934/1/012015. URL <http://stacks.iop.org/1742-6596/934/i=1/a=012015?key=crossref.c7b72e42c6b48a5cdb06944fcba094a11>
- [5] E. S. Seo, et al., Cosmic Ray Energetics And Mass for the International Space Station (ISS-CREAM), Advances in Space Research 53 (10) (2014) 1451–1455. doi:10.1016/j.asr.2014.01.013. URL <http://www.sciencedirect.com/science/article/pii/S02731177140000313>
- [6] E. C. Stone, et al., Voyager 1 Observes Low-Energy Galactic Cosmic Rays in a Region Depleted of Heliospheric Ions, Science 341 (6142) (2013) 150–153. doi:10.1126/science.1236408. URL <http://science.scienmag.org/content/341/6142/150>
- [7] D. Hovestadt, et al., A detector system for cosmic ray electrons, Nuclear Instruments and Methods 85 (1) (1970) 93–100. doi:10.1016/0029-554X(70)90125-4. URL <http://www.sciencedirect.com/science/article/pii/0029554X70901254>
- [8] J. M. Clem, et al., Solar Modulation of Cosmic Electrons, The Astrophysical Journal 464 (1996) 507. doi:10.1086/177340. URL <http://adsabs.harvard.edu/abs/1996ApJ...464..507C>
- [9] P. Evenson, et al., Cosmic Ray Electron Spectrum in 2009 (2009) 5.
- [10] O. Adriani, et al., An anomalous positron abundance in cosmic rays with energies 1.5–100GeV, Nature 458 (2009) 607. URL <http://dx.doi.org/10.1038/nature07942>
- [11] T. F. L. Collaboration, M. Ackermann, et al., Measurement of separate cosmic-ray electron and positron spectra with the Fermi Large Area Telescope, Physical Review Letters 108 (1), arXiv: 1109.0521. doi:10.1103/PhysRevLett.108.011103. URL <http://arxiv.org/abs/1109.0521>
- [12] M. Tanabashi, et al., Review of particle physics, Phys. Rev. D 98 (2018) 030001. doi:10.1103/PhysRevD.98.030001. URL <https://link.aps.org/doi/10.1103/PhysRevD.98.030001>
- [13] H. Kelley, G. Alonso, Ltc6244 high speed peak detector, <https://www.analog.com/en/technical-articles/ltc6244-high-speed-peak-detector.html>, accessed: 2022-09-23.
- [14] Slerj, SSR-LC User's Manual, rev. E (Sep 2019).
- [15] Design of permanent multipole magnets with oriented rare earth cobalt material 169 (1). doi:10.1016/0029-554X(80)90094-4. URL <http://www.sciencedirect.com/science/article/pii/0029554X80900944>
- [16] W. Atwood, et al., Design and initial tests of the Tracker-converter of the Gamma-ray Large Area Space Telescope, Astroparticle Physics 28 (4-5) (2007) 422–434. doi:10.1016/j.astropartphys.2007.08.010. URL <http://linkinghub.elsevier.com/retrieve/pii/S0927650507001302>
- [17] R. P. Johnson, et al., Tracker Readout ASIC for Proton Computed Tomography Data Acquisition, IEEE transac-

- 625 tions on nuclear science 60 (5 Pt 1) (2013) 3262–3269.
doi:10.1109/TNS.2013.2274663.
- 630 URL <https://www.ncbi.nlm.nih.gov/pmc/articles/PMC3957097/>
- [18] R. P. Johnson, et al., A Fast Experimental Scanner for Proton
635 CT: Technical Performance and First Experience With Phantom Scans, IEEE Transactions on Nuclear Science 63 (1) (2016)
52–60. doi:10.1109/TNS.2015.2491918.
- [19] J. D. Sullivan, Geometrical factor and directional response of
635 single and multi-element particle telescopes, Nuclear Instruments and Methods 95 (1971) 5. doi:10.1016/0029-554X(71)
90033-4.
URL <http://adsabs.harvard.edu/abs/1971NucIM..95....5S>
- [20] R. Fröhlich, Application of kalman filtering to track and vertex fitting, Nuclear Instruments and Methods in Physics Research Section A: Accelerators, Spectrometers, Detectors and Associated Equipment 262 (2) (1987) 444 – 450. doi:[https://doi.org/10.1016/0168-9002\(87\)90887-4](https://doi.org/10.1016/0168-9002(87)90887-4).
URL <http://www.sciencedirect.com/science/article/pii/0168900287908874>
- 645 [21] V. Khachatryan, et al., Measurement of the charge ratio of atmospheric muons with the CMS detector, Physics Letters B 692 (2) (2010) 83–104. doi:10.1016/j.physletb.2010.07.033.
URL <http://www.sciencedirect.com/science/article/pii/S0370269310008725>